ACS OMEGA

http://pubs.acs.org/journal/acsodf

Article

Influences of Ferric Ions and Fe as a Minor Element in the Lattice on the Floatability of Cassiterite

Haosheng Wu,* Doreen Ebert, Robert Möckel, Kai Bachmann, Axel D. Renno, and Martin Rudolph

Cite This: *ACS Omega* 2023, 8, 5702−5714

Read Online

ACCESS | Metrics & More | Article Recommendations

ABSTRACT: In this study, synthetic pure cassiterite and cassiterite doped with two different Fe contents were successfully recrystallized by means of sintering. Their crystal structure and chemical compositions were characterized by X-ray powder diffraction (XRD) as well as scanning electron microscopy (SEM) combined with energy-dispersive X-ray (EDX) analysis. Their floatability was studied by microflotation with a diphosphonic acid surfactant named Lauraphos301 as a collector. Unlike the addition of ferric ions in solution, which strongly depressed the floatability of all of the cassiterite samples, a much higher flotation efficiency of the Fe-doped cassiterite samples was found especially at lower collector concentrations. The cassiterite floatability is proportional to the Fe content in cassiterite at a broad range of pH, and the recovery has the following order: cassiterite with 1417 ppm Fe > cassiterite with 1165 ppm Fe > pure cassiterite. The electrokinetic behavior of the cassiterite samples with and without the collector was studied by electrophoretic measurements and revealed that the chemical interaction dominated the adsorption. With the help of the particle shape analysis, a more angular shape was found for the Fe-doped cassiterite samples. Moreover, without the influence of particle shape, much abundant adsorption of Lauraphos301 was found on the Fe-doped cassiterite samples by AFM topography imaging. The minor amount of Fe in the cassiterite lattice and a more angular shape of the Fe-doped cassiterite samples were believed to enhance floatability collectively. The study reveals that the influence of the chemical composition of the minerals on flotation was almost inextricably bound up with particle morphology and emphasizes the importance of considering both factors and investigating them individually for the flotation study.

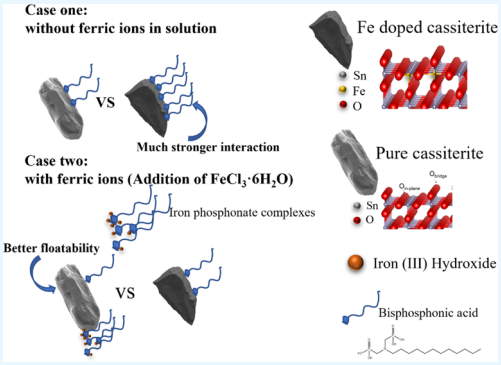

1. INTRODUCTION

Surfactant adsorption on particles and particle interactions with air bubbles in aqueous solutions are both of academic and practical significance, which also belong to very important subprocesses in froth flotation. Froth flotation is a complex heterocoagulation separation process. Hydrophobized mineral particles of interest collide and attach to air bubbles within an intensively mixed pulp and are then transported out of the pulp into an upper froth phase, in which the mineral of interest is concentrated and can be recovered.[1] Out of the well-established approaches to increase flotation efficiency, a significant amount of research work on adjusting the surface properties of the mineral has been reported in the past four to five decades.[2−5] These include a constant development of novel types of surfactants (commonly called flotation collectors) to improve the adsorption efficiency, selectivity, and consequently adhesion to air bubbles. For nonsulfidic minerals, selective hydrophobization can be achieved by (i) adjusting the pH increasing the electrostatic interactions between collectors and minerals as well as between minerals and bubbles;[6,7] (ii) controlling ion speciation in the pulp,[8−11] etc. Investigation of individual particle properties, e.g., chemical composition, is thus of fundamental importance to enhance our understanding of the flotation behavior.

An economically important mineral often beneficiated through froth flotation is cassiterite (SnO_2) as the main carrier of tin for various industrial applications. In nature, there is no pure SnO_2 to be found. More than 15 elements have been found within the cassiterite lattice from 26 different mineral deposits, the most common being Fe, Ti, W, Ta, Zr, Nb, Mn, and Sc.[12−15] Cassiterite from different deposits often exhibits quite different flotation properties.[16−19] Some tin ore types have such significant differences that even within one deposit, the cassiterite flotation behaves differently.[20,21] The understanding of various influencing factors was developed during the last decades, but the influence of lattice impurity in cassiterite had barely been mentioned, and the reported studies show

Received: November 10, 2022
Accepted: January 5, 2023
Published: February 2, 2023

contradictory conclusions. The earliest attempt to produce synthetic cassiterite for fundamental flotation investigations has been reported in 1950. Schuman and Prakash[22] produced tin oxide through the hydrolysis of $SnCl_4$ at high temperatures. They have found that pure cassiterite floats without any contamination easily over a wide range of pH values. Sutherland and Wark[23] produced SnO_2 by heating and annealing the H_2SnO_3 solution. They have found that pure cassiterite cannot be floated using fatty acid as a collector. Gruner[24] used a chemical transport reaction to produce pure cassiterite as well as Fe-, Mn-, Ca-, Ti-, Si-, and Al-doped cassiterite, and used different alkyl phosphonic acids as collectors for the flotation test. The results had shown that pure cassiterite had the best flotation behavior over a broad pH range. On the other hand, Balachandran used sintering to produce pure and Fe- and Sb-doped cassiterite.[25] The flotation results had shown that Fe-doped cassiterite has a much better floatability compared to pure cassiterite both using sodium dodecyl sulfate and dodecyl ammonium acetate as collectors.

Even though the samples' chemical composition has been well described in these studies, the particle properties had barely been addressed. Besides the chemical composition, the particle size, particle shape, and particle surface roughness also play a crucial role in the various subprocesses in flotation, including the following effects: (i) the induction time for particle−bubble attachment is partly governed by particle shape;[26] (ii) the adsorption density of flotation reagents on mineral particles is also affected by particle shape, and (iii) the wettability and floatability of minerals are affected by particle roughness.[27] It is thus important to analyze the particle flotation behavior not only characterizing the chemical composition but also the macroscopic physical properties, e.g., particle surface topography and particle geometry (morphology).

In this study, the aim is thus made to understand the influence of Fe as an important minor element in various local ores of the Erzgebirge mountains in Germany on the floatability of cassiterite. The ferric ions' influence on the floatability of cassiterite is also taken into investigation. Diphosphonic acid Lauraphos301 was applied as a collector in the microflotation test. Sintering was chosen for this study due to its possibility of producing sufficient amounts of single crystals for the flotation test with a rather homogeneous composition. The synthesized samples were physically and chemically characterized at different size fractions. Their floatability and ζ potential were compared. Furthermore, to exclude the effect of surface roughness and particle geometry, the adsorption of Lauraphos301 on samples was characterized with the help of AFM topography analysis on samples with and without Lauraphos301.

2. RESULTS AND DISCUSSION

2.1. Substitution of Fe in the Cassiterite Lattice. The crystallographic structure of cassiterite is ditetragonal−dipyramidal, which is characterized by two lattice parameters, *a* and *c*. As shown in Table 1, the lattice constants of pure cassiterite and Fe-doped cassiterite are similar, but Fe-doped cassiterite holds a slightly higher lattice constant. As the crystal radius of the 4-coordinated Sn^{4+} is 0.69 Å and that of Fe^{3+} is 0.92 Å,[28] a slightly larger lattice constant indicated a successful substitution of Fe in the cassiterite lattice.

Table 1. Lattice Constants (nm) of Pure Cassiterite and Cassiterite Doped with Lower Fe Content Measured by X-ray Powder Diffraction (XRD)

	a	*c*
pure cassiterite	0.47377(1)	0.31867(1)
Fe-doped cassiterite	0.47379(1)	0.31869(1)

Based on the EDX analysis, cassiterite doped with low Fe content contains 1165 ± 297 ppm of Fe. Cassiterite doped with high Fe content contains 1417 ± 324 ppm. Only Sn and O elements were detected by SEM−EDX measurement in pure cassiterite.

2.2. Flotation Behavior Comparison between Pure Cassiterite and Fe-Doped Cassiterite. To determine the ideal pH and concentration of Lauraphos301 as a collector, Lauraphos301 concentration from 1×10^{-5} to 1×10^{-3} mol L^{-1} at pH 6.8 as well as a Lauraphos301 concentration of 1×10^{-4} mol L^{-1} at a pH range from 3 to 9 were studied during the microflotation test. The microflotation recovery of pure cassiterite and cassiterite with 1417 and 1165 ppm Fe as a function of Lauraphos301 concentration in the range of 1×10^{-5} to 1×10^{-3} mol L^{-1} at pH 6.8 is shown in Figure 1. A clear trend can be seen that within the investigated collector concentration, the recovery of the cassiterite samples increased with the Fe content in cassiterite at pH 6.8. With 1×10^{-5} mol L^{-1} Lauraphos301, the recovery of cassiterite with 1417 ppm Fe could reach already 76% at pH 6.8, while for pure cassiterite, the recovery was only 31.5%. A general higher recovery of all cassiterite samples was reached at the collector concentration of 1×10^{-3} mol L^{-1}. However, at such a high concentration, a denser froth was noticed. The much higher recovery, especially for pure cassiterite is thus believed to be due to a much denser froth, which leads to the continuous mechanical transport of particles, i.e., entrainment. As for cassiterite with 1417 ppm Fe, there is no significant difference between the recovery from 1×10^{-5} to 1×10^{-3} mol L^{-1}. A concentration of 1×10^{-4} mol L^{-1} was thus chosen for further microflotation measurement to study the suitable pH range using Lauraphos301 as a collector.

Figure 2 represents the microflotation recovery of pure cassiterite and cassiterite with 1417 and 1165 ppm Fe as a function of pH in the range of 3−9 using 1×10^{-4} mol L^{-1} Lauraphos301 as a collector. Higher recovery of Fe-doped cassiterite can also be seen within the investigated pH range, and the recovery increase is proportional to the Fe content in cassiterite. Also, it is noticed that in the pH range between 3 and 6, recovery of all of the cassiterite samples increased. The maximum recovery of all of the cassiterite samples was reached at pH 6, and the recovery of cassiterite with 1417 ppm Fe with a value of 82% achieved the highest recovery value, at which the dominating species of Lauraphos301 is the nondissociated species R-N-$(CH_2\text{-}H_2PO_3)_2$. Within the pH range, nondissociated species decreased while monoanion R-N-$[(CH_2\text{-}HPO_3)_2]^{2-}$ increased.

Furthermore, to study the influence of ferric ions on the floatability of cassiterite using Lauraphos301 as a collector, microflotation of pure cassiterite and cassiterite with 1165 pm Fe with 2×10^{-4} mol L^{-1} Fe^{3+} in solution at a pH range from 3 to 11 was further carried out. While Fe as a minor element vastly enhanced the cassiterite floatability, ferric ions strongly depressed the floatability of cassiterite, as shown in Figure 3. The depressing effect of Fe^{3+} could be explained as follows: based on the Lewis theory of acids and bases, Fe^{3+} being a strong acid prefers to combine with strong base ligands containing the phosphonic group, which interact thus intensively with the Lauraphos301 forming complexes leading to lower adsorption

https://doi.org/10.1021/acsomega.2c07230
ACS Omega 2023, 8, 5702−5714

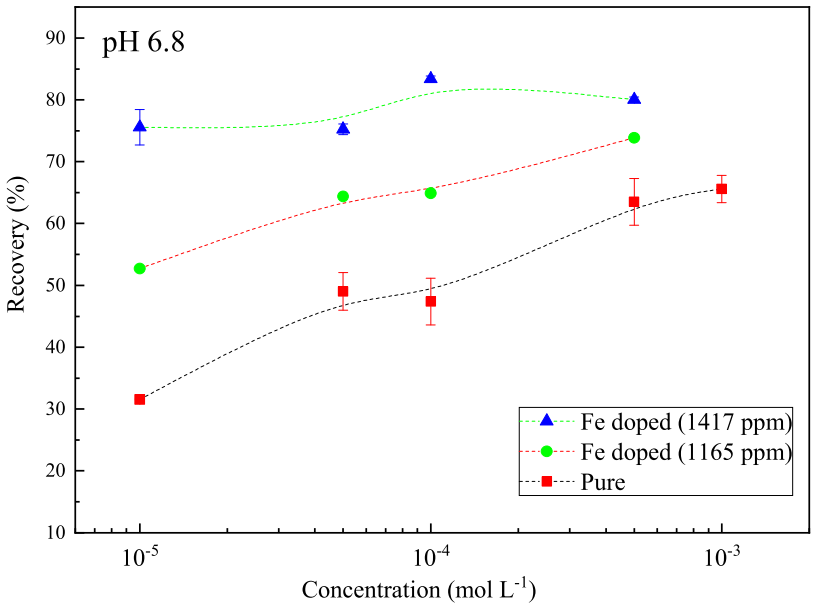

Figure 1. Microflotation recovery of pure cassiterite and cassiterite containing 1417 and 1165 ppm Fe as a function of Lauraphos301 concentration in the range of 10^{-5} to 10^{-3} mol L^{-1} for the fixed particle size range of 32−40 μm at pH 6.8. Each measurement point represents the average value of at least three repeat measurements with error bars showing the standard deviations. (For those without an error bar, the measurement was performed only once). The dash-dotted lines in the figure are guides for the eye.

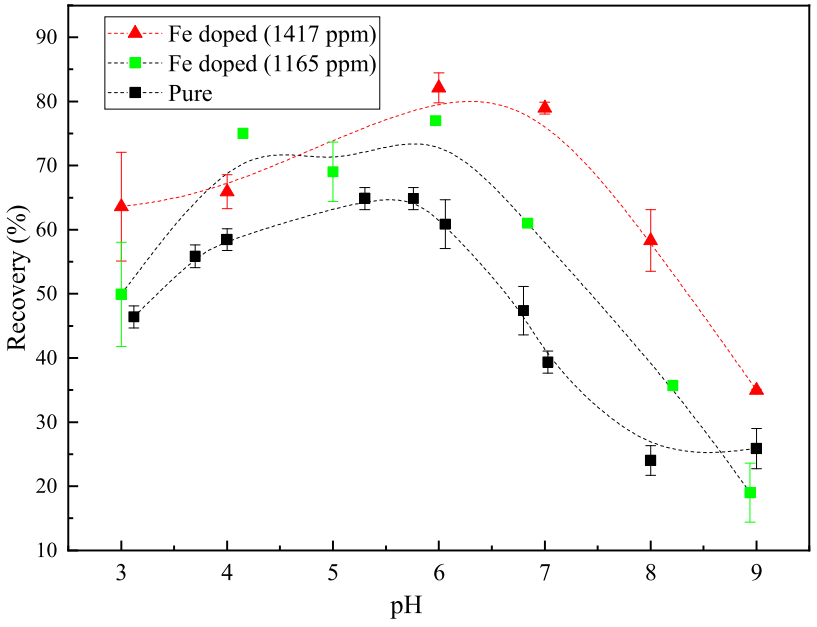

Figure 2. Microflotation recovery of pure cassiterite and cassiterite with 1417 and 1165 ppm Fe as a function of pH from 3 to 9 with 1×10^{-4} mol L^{-1} Lauraphos301 as a collector. Each measurement point represents the average value of at least three repeat measurements with an error bar showing the standard deviation. (For those without an error bar, the measurement was performed once). The dash-dotted lines in the figure are guides for the eye.

of Lauraphos301 on cassiterite samples. The formation of the iron phosphonate complex and the strong depressant effect of ferric ions on cassiterite flotation using phosphonic acid was also well reported by other studies.[20,29−32]

It is, however, worth noting that the influence of Fe^{3+} ions on Fe-contained cassiterite is even more stronger than on pure cassiterite. From a wide range of pH values, the recovery of Fe-doped cassiterite remained lower than 30%, while the recovery of pure cassiterite could still reach around 55% in a less acidic pH range from 7 to 9. In this pH range, hydroxy complexes $Fe(OH)^{2+}$ and $Fe(OH)^{2+}$ are the most abundant species. Based on the observation during the flotation measurement (see Appendix), it is thus believed that the hydroxy complexes tend to attach to pure cassiterite while not to Fe-doped cassiterite. Meanwhile, the hydroxy complexes interacted with phosphonic acid and formed iron phosphonate complexes on the particle surfaces, which increased the hydrophobicity, i.e., the decreased surface energy of pure cassiterite. It enhances not only the attachment of pure cassiterite toward bubbles but also the attachment between pure cassiterite particles and formed macroscopically brown flocculants.

https://doi.org/10.1021/acsomega.2c07230
ACS Omega 2023, 8, 5702−5714

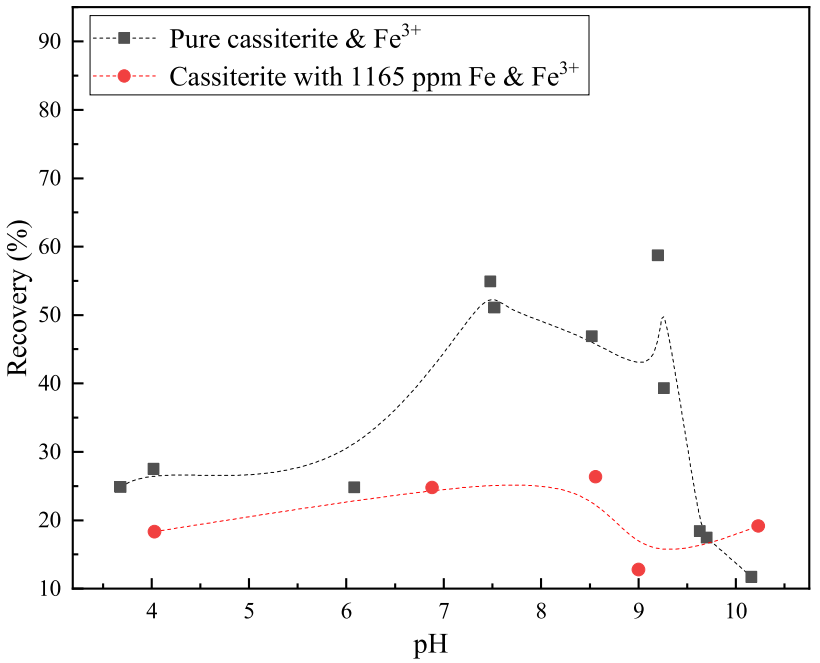

Figure 3. Microflotation recovery of pure cassiterite and cassiterite with 1165 ppm Fe as a function of pH from 3 to 10; 1×10^{-4} mol L^{-1} Lauraphos301 was used as a collector with 2×10^{-4} mol L^{-1} Fe^{3+} in the solution. Each measurement point represents one microflotation measurement. The dash-dotted lines in the figure are guides for the eye.

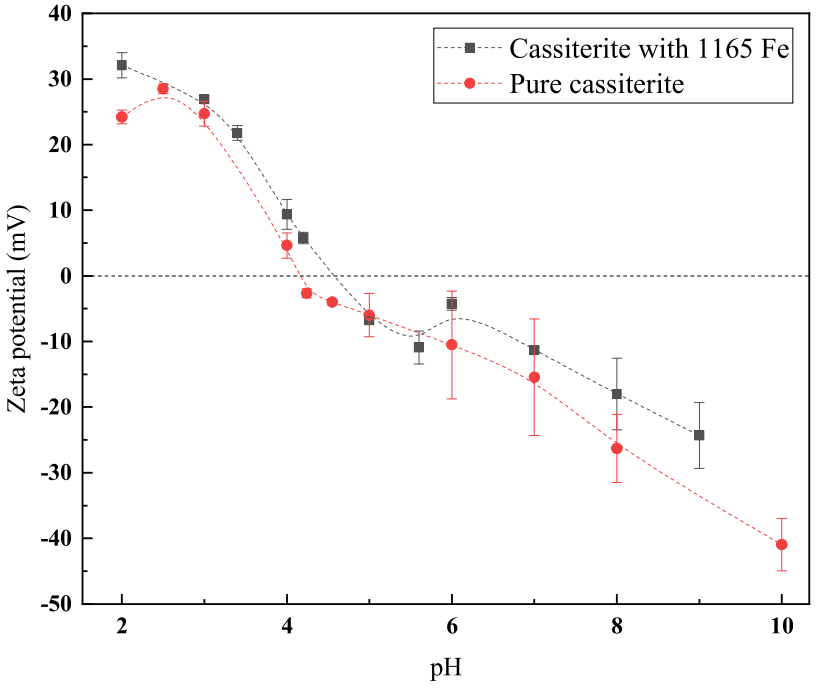

Figure 4. ζ potentials of pure cassiterite and cassiterite with 1165 ppm Fe calculated by electrophoretic mobility measurements as a function of pH in the range from 2 to 10 within 10 mM KCl background solution. Each plotted data point is the average value of three measurements consisting of 50 subruns with error bars showing the standard deviation. The dash-dotted lines in the figure are guides for the eye.

2.3. Adsorption Mechanism of Lauraphos301. To investigate the interaction between cassiterite and Lauraphos301, a range of ζ potential measurements of cassiterite samples with and without the presence of Lauraphos301 was further conducted. As shown in Figure 4, the isoelectric point (IEP) of pure cassiterite was within 4.0−4.1, while cassiterite with 1165 ppm Fe increased its IEP to 4.3−4.4. The measured isoelectric point of pure SnO_2 is highly consistent with the formerly produced sample.[33] Also, the measured IEP agrees with the other studies.[34] It is noticed that ζ potential differences between the two cassiterite samples are insignificant, but a trend can be seen that Fe-doped cassiterite has a slightly higher ζ potential at the positively charged range and a lower value in the negatively charged range.

Furthermore, ζ potentials of pure cassiterite and cassiterite with 1165 ppm Fe in the presence of 1×10^{-6} mol L^{-1} to $1 \times$

https://doi.org/10.1021/acsomega.2c07230
ACS Omega 2023, 8, 5702−5714

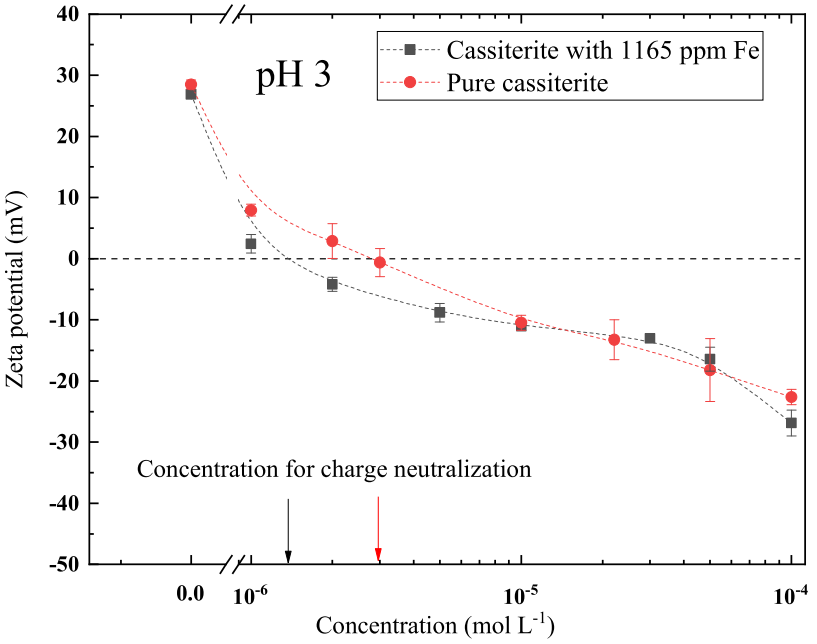

Figure 5. ζ potentials of pure cassiterite and cassiterite with 1165 ppm Fe calculated by electrophoretic mobility measurements as a function of Lauraphos301 within the concentration from 1×10^{-6} to 1×10^{-4} mol L^{-1} at pH 3. Each plotted data point is the average value of three measurements consisting of 50 subruns with an error bar showing the standard deviation. The dash-dotted lines in the figure are guides for the eye.

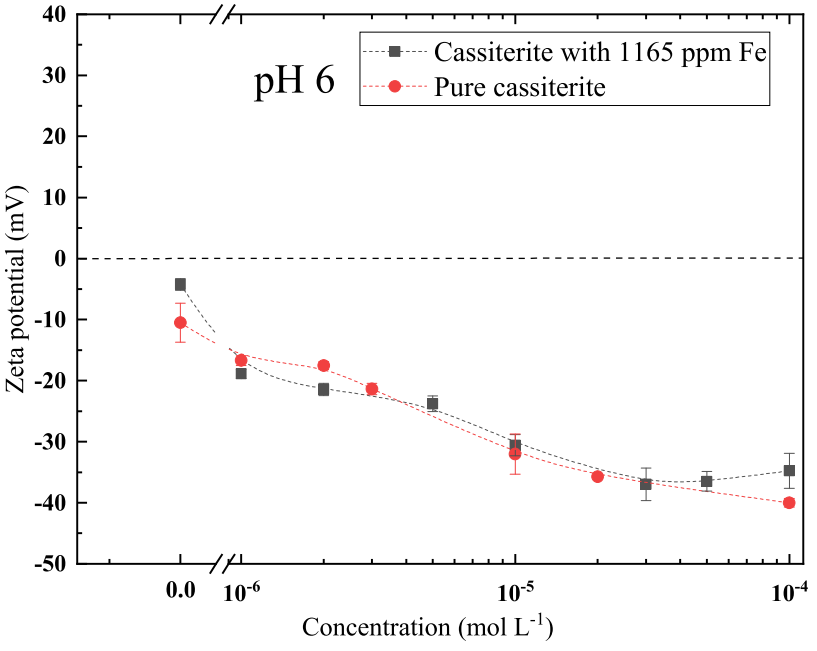

Figure 6. ζ potentials of synthesized pure cassiterite and Fe-doped cassiterite calculated by electrophoretic mobility measurements as a function of Lauraphos301 within the concentration range from 10^{-6} to 10^{-4} mol L^{-1} at pH 6. Each plotted data point is the average value of three measurements consisting of 50 subruns with an error bar showing the standard deviation. The dash-dotted lines in the figure are guides for the eye.

10^{-4} mol L^{-1} Lauraphos301 at pH 3 were measured, and the results are shown in Figure 5. It can also be seen in Figure 5 that without the presence of Lauraphos301, the two cassiterite samples held almost the same ζ potential with 25 mV for pure cassiterite and 27 mV for cassiterite with 1165 ppm Fe. With the addition of 1×10^{-6} to 1×10^{-5} mol L^{-1} Lauraphos301 in the solution, the ζ potential of cassiterite with 1165 ppm Fe decreased stronger than pure cassiterite. At pH 3, the existing species of Lauraphos301 in the solution are the nondissociated species R-N-$(CH_2\text{-}H_2PO_3)_2$ and the negatively charged monoanion R-N-$[(CH_2\text{-}HPO_3)_2]^{2-}$. The more substantial decrease of ζ potential of cassiterite with 1165 ppm Fe indicates more abundant adsorption of the negatively charged monoanion R-N-$[(CH_2\text{-}HPO_3)_2]^{2-}$ and most likely also the nondissociated species R-N-$(CH_2\text{-}H_2PO_3)_2$ on it. Also, it is worth noting that cassiterite with 1165 ppm Fe reached charge neutrality with the presence of 1.5×10^{-6} mol L^{-1} Lauraphos301, while it needs almost 3×10^{-6} mol L^{-1} Lauraphos301 for pure cassiterite. At the charge neutralization point, bilayers of Lauraphos301 are believed to generate on the cassiterite samples, as it is well

https://doi.org/10.1021/acsomega.2c07230
ACS Omega 2023, 8, 5702−5714

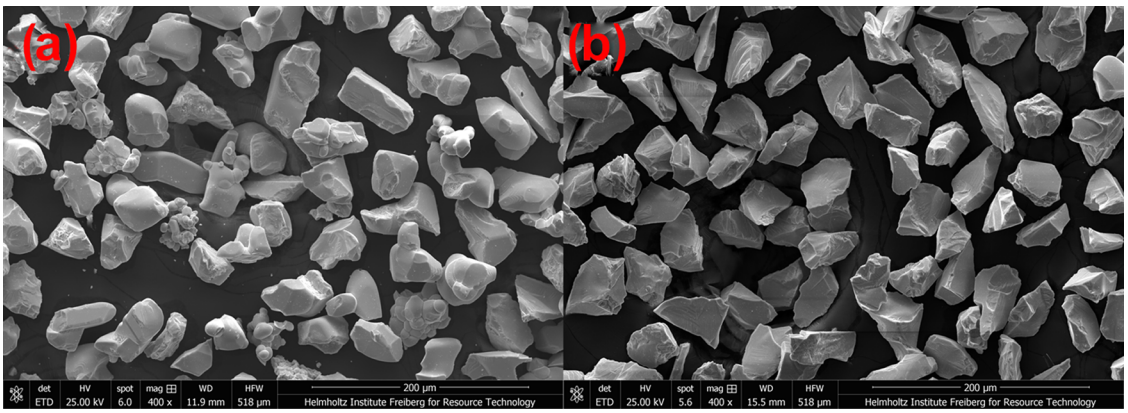

Figure 7. Secondary electron (SE) image of (a) pure cassiterite particles and (b) Fe-doped cassiterite particles within the size fraction 32−40 μm.

reported[35−37] that the ζ potential of the solid reverses its sign as the bilayer develops on the solid−liquid interface. Afterward, the adsorption of surfactant for the formation of bilayers or even multilayers is not dependent on the solid property but rather on the surfactant itself (tail−tail interactions). The result shown in Figure 5 matches with the earlier study that there was no significant difference between the ζ potential of the two samples when the concentration of Lauraphos301 in solution was larger than 1×10^{-5} mol L^{-1}, at which it is believed that the bilayer or even multilayer of Lauraphos301 was generated on the sample surface.

The adsorption behavior of Lauraphos301 on samples was also investigated at pH 6 as at this pH, the microflotation of all of the cassiterite samples reached their maximal recovery. Figure 6 represents the ζ potential of pure cassiterite and cassiterite with 1165 ppm Fe without Lauraphos301 and as a function of Lauraphos301 within the concentration from 10^{-6} to 10^{-4} mol L^{-1} at pH 6. Compared to pure cassiterite a more substantial decrease of the ζ potential of cassiterite with 1165 ppm Fe was again observed by adding a lower amount of Lauraphos301 in the solution, i.e., at 1×10^{-6} mol L^{-1}. Since at pH 6 both the solid and surfactant are negatively charged, it is difficult to tell at which concentration the Luaraphos301 reaches the generation of bilayers on the solid−liquid interface and starts to build up solid property nonrelated multilayers. However, based on what was observed at pH 3, the assumption is made that at the concentration where the two samples start to hold similar ζ potential, i.e., at around 5×10^{-6} mol L^{-1}, a generation of bilayer or even multilayer adsorption already exists, as can be seen in Figure 6, which is much less than the concentration needed at pH 3. It indicates a general more abundant adsorption of Lauraphos301 at pH 6, which also matched with the microflotation result. Moreover, it is thus believed that the adsorption of the negatively charged monoanion R-N-$[(CH_2\text{-}HPO_3)_2]^{2-}$ is more abundant on cassiterite with 1165 ppm Fe when the concentration of Lauraphos301 has not yet reached the generation of the bilayer.

It is worth mentioning that the dissociation constants of Lauraphos301 are pK_{a1} = 6.8 and pK_{a2} = 8.8. The maximum recovery of all of the cassiterite samples using Lauraphos301 arrived at pH 6, which is near the equilibrium point between the nondissociated and the monoanion species of Lauraphos301. The first well-reported phosphonic acid for cassiterite flotation, styrene phosphonic acid (SPA), holds quite different dissociation constants: pK_{a1} = 2 and pK_{a2} = 7.0.[38] Senior[21] reported that for well acid-leached natural cassiterite samples (indicating no ion influence), the pH of maximum recovery using SPA as a collector is around pH 2, which is also near the equilibrium point between the nondissociated and the monoanion species of SPA.

Wottgen[39] and Gruner[40] elucidated the maximum adsorption of SPA around pH 2 on cassiterite due to increased electrostatic attraction between partially dissociated phosphonic acid and the positively charged mineral surface below the isoelectric point; while Fuerstenau and Healy[41] held the opinion that coadsorption of undissociated phosphonic acid was the mechanism responsible for adsorption increase. Also, the chemical interaction between styrene phosphonic acid and oxide minerals has been studied by Kuys et al.[42] They analyzed the adsorption mechanism of SPA by FTIR-ATR and concluded that the Sn^{4+} and SPA chemically interacted with each other in the pH range of 2.3−7.5, while the strongest adsorption happens between pH 4.5 and 5.5. Farrow et al.[38] further studied the adsorption mechanism between SPA and the stannic oxides using three independent measurements, including adsorption isotherms measurement, ζ potential determination, and hydroxyl ions relation from the stannic oxide during SPA uptake at pH 3−5. The results proved that chemical interaction plays a very important role in the interaction between the phosphonic functional group and cassiterite.

For the case of Lauraphos301 in this study, the pH of monoanionic R-N-$[(CH_2\text{-}HPO_3)_2]^{2-}$ increased from 3 to 6, as can be seen from the titration result shown in Figure 11. Regardless of the changing of the surface potential from positive to negative, which makes the potential physical adsorption less favorable, stronger adsorption at pH 6 reveals that chemical adsorption of Lauraphos301 on cassiterite is more likely to be involved in the interaction, and the results supported the proposal of Fuerstenau and Healy that the coadsorption of the nondissociated species R-N-$(CH_2\text{-}H_2PO_3)_2$ and the monoanionic R-N-$[(CH_2\text{-}HPO_3)_2]^{2-}$ plays an important role in the interaction with cassiterite.

2.4. Particle Shape Influence on Cassiterite Floatability. It is well known from the former studies that particle morphology, especially the shape and particle surface roughness,[43] plays a crucial role in the various subprocesses in flotation, in which the particle−bubble and particle−particle interactions are significant. The influence of the particle shape and roughness on cassiterite flotation was thus investigated.

The secondary electron (SE) images in Figure 7 show an overview of the shape difference between pure and Fe-doped cassiterite samples within the size fraction of 32−40 μm. As can be seen from Figure 7, the particle size distribution is very

https://doi.org/10.1021/acsomega.2c07230
ACS Omega 2023, 8, 5702−5714

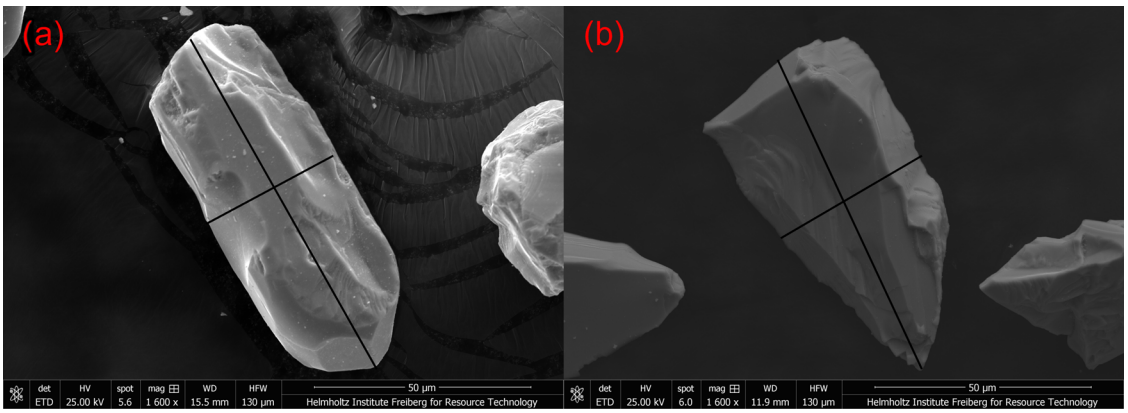

Figure 8. Secondary electron (SE) image of (a) one pure cassiterite particle and (b) one Fe-doped cassiterite particle (Fe content, 1165 ppm).

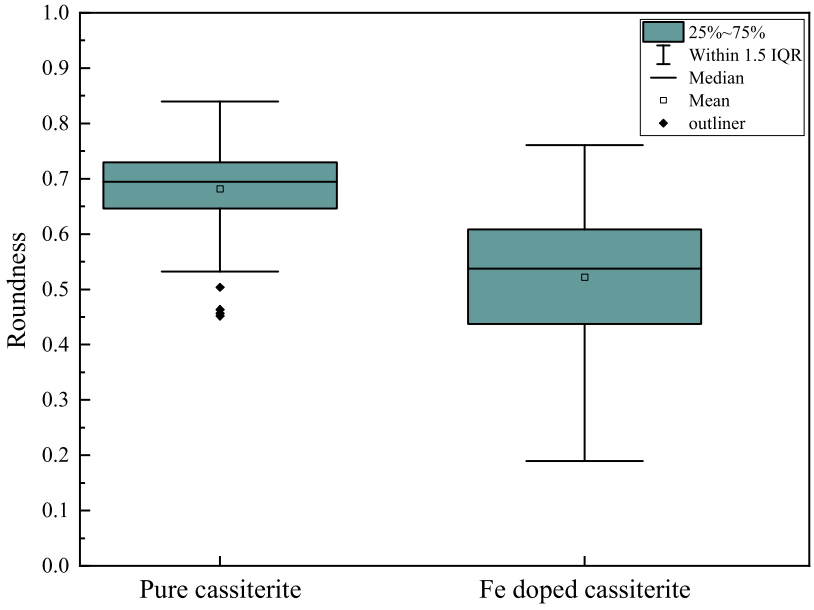

Figure 9. Comparison of roundness distribution between pure cassiterite and cassiterite with 1165 ppm Fe.

similar. Also, based on the morphology and structure of one pure as well as one Fe-doped cassiterite particle observed in SE images in Figure 8 and the same grinding procedure for all of the cassiterite samples with similar hardness, it is believed that the surface roughness of the cassiterite particle should be similar and would not play an essential role in this study.

However, it can be noted that pure and Fe-doped cassiterite hold slightly different particle shapes. The SE images in Figure 8 with a larger magnification also show that the particle edge of Fe-doped cassiterite is sharper than pure cassiterite. The difference was believed to be the enhancement of mass transport at grain boundary due to the addition of dopant with lower valence during sintering, which led to densification and growth of larger polycrystalline oxides, which was reported by Varela et al.[44]

The roundness of pure cassiterite and cassiterite with 1165 ppm Fe were calculated. The results as presented in Figure 9 show that pure cassiterite ($R_{average}$ = 0.68) is rounder than cassiterite with 1165 ppm Fe ($R_{average}$ = 0.53). For single oxide mineral systems (e.g., alumina, quartz), many studies have reported that the more angular the minerals, the higher the recovery of the minerals.[45−47] It is thus reasonable to believe that the more prismatic and angular shape of the Fe-doped cassiterite samples also contributes to the higher recovery of Fe-doped cassiterite.

Since the earliest attempt to produce synthetic cassiterite for the chemical composition study in 1950,[22] there have been quite a few studies focusing on the minor element influence on cassiterite flotation and have contradictory conclusions. Also, our former attempt to use phosphonic acid also (styrene phosphonic acid, SPA) as a collector[33] has quite the opposite result that pure cassiterite has the highest flotation recovery compared to Fe-doped cassiterite and natural cassiterite (enriched with Fe). One crucial influence factor that was neglected in our former study is the particle shape. Even though the particle size distribution was quite similar, since no wet sieving was involved for sample preparation, a small amount of very fine but flat particles were in the sample, especially in pure cassiterite, which is believed is also the case in the study by Gruner[24] as well as Schumann and Prakash.[22] Such flat particles serve as surfactants and can float without adding an extra collector, which leads to thus the misleading result that pure cassiterite can float. Also, in the study of particle shape, studies report opposite results that the rounder the particle, the higher the recovery,[43,48] in which a more complex system containing natural minerals with large chemical composition differences

https://doi.org/10.1021/acsomega.2c07230
ACS Omega 2023, 8, 5702−5714

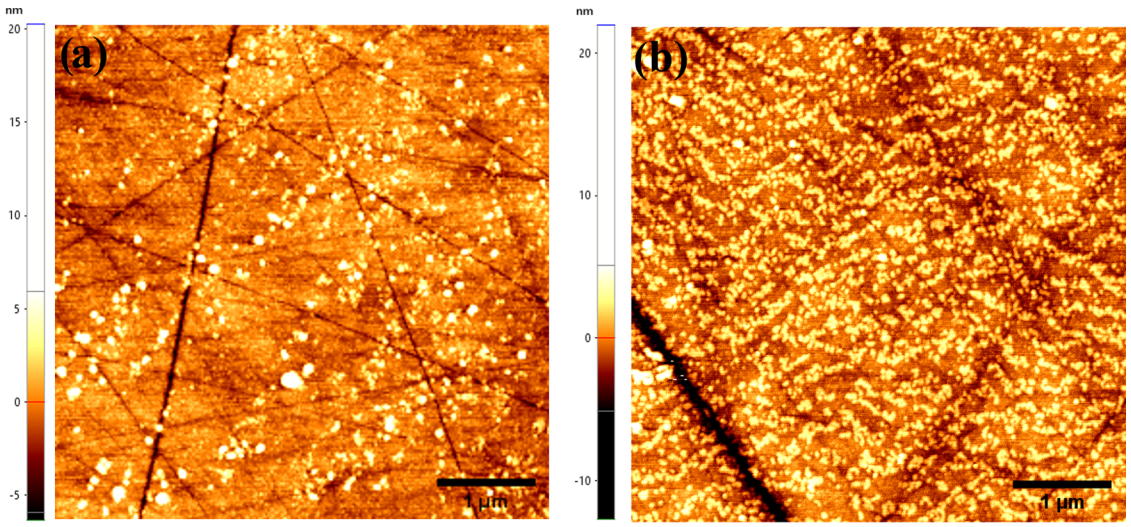

Figure 10. AFM topography of (a) pure cassiterite and (b) cassiterite with 1417 ppm Fe treated with 1×10^{-4} mol L^{-1} Lauraphos301 at pH 6.

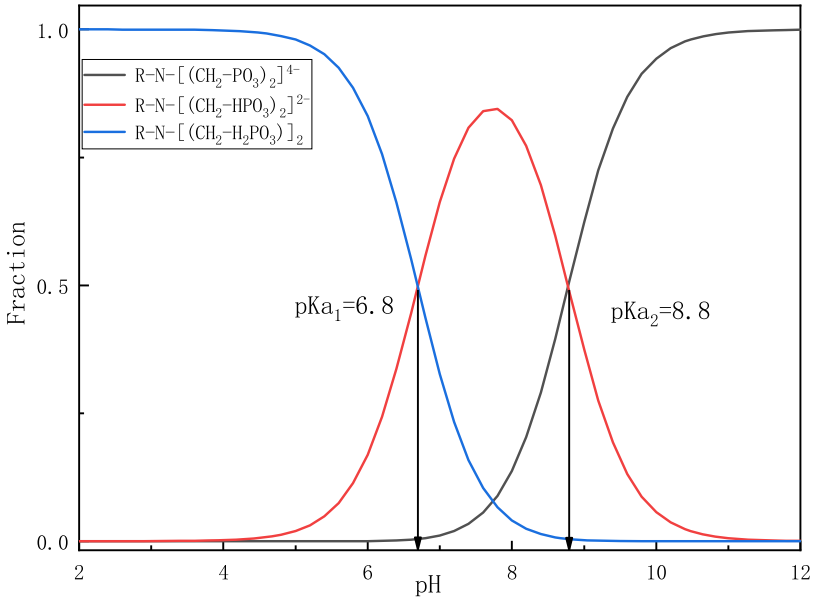

Figure 11. Distribution of species of the diphophonic acid Lauraphos301 (CAS number 3015995-33-5).

between each crystal structure is involved. To further find out the influence of Fe as a minor element in cassiterite, it is thus important to study the chemical composition exclusively.

2.5. Influence of Fe as a Minor Element on Cassiterite Floatability. To study the influence of the chemical composition difference exclusively, atomic force microscopy measurement was further carried out. The roughness of pure cassiterite and cassiterite with 1417 ppm Fe was first measured. The topography of the two samples is shown in the Appendix in Figure 16. The root mean square of the measured height Sq of a 5 μm × 5 μm area for pure cassiterite is 0.7 ± 0.05 nm, and for cassiterite with 1417 ppm Fe is 0.6 ± 0.08 nm. No significant difference can be seen between the two samples. Also, during the topography scanning, areas with noticeable deep scratches were intentionally avoided. The roughness effect can thus be neglected. As shown in Figure 10, a noticeable adsorption difference of Lauraphos301 between the two samples can be seen. The adsorption of Lauraphos301 on cassiterite with 1417 ppm Fe is more abundant than that on pure cassiterite.

With the help of the AFM topography measurement, a conclusion can be drawn that Fe as a minor element in the cassiterite lattice does enhance the adsorption of phosphonic acid as a collector.

4. CONCLUSIONS

Based on the SEM−EDX and XRD measurements, a range of pure cassiterite and cassiterite doped with two different amounts of Fe were successfully recrystallized by means of sintering. The microflotation results have proven that, unlike the ferric ions, which strongly depress the recovery of cassiterite, Fe as a minor element in cassiterite has enhanced the cassiterite flotation intensively using diphosphonic acid as a collector. Results have shown that compared to the pure cassiterite sample, the Fe-doped cassiterite samples have a much higher flotation recovery in a wide range of pH values, especially at a low collector concentration of 10^{-6} mol L^{-1}. The result of the ζ potential measurement confirmed further much stronger adsorption of Lauraphos301 on the Fe-doped cassiterite sample. Also, with the

https://doi.org/10.1021/acsomega.2c07230
ACS Omega 2023, 8, 5702−5714

help of the ζ potential measurement, a better understanding of the adsorption mechanism is gained that the chemical reaction should be the dominant reaction; also, the results supported the proposal of Fuerstenau and Healy[49] that the coadsorption of the nondissociated species (in this case, R-N-$(CH_2\text{-}H_2PO_3)_2$ and monoanionic R-N-$[(CH_2\text{-}HPO_3)_2]^{2-}$) takes an essential role in the interaction with cassiterite.

With the help of the particle shape and the AFM topography analysis, it is believed that a much higher flotation efficiency of Fe-doped cassiterite, especially at a lower collector concentration, is due to the minor amount of Fe in the cassiterite lattice as well as the more angular particle shape. The study reveals that the influence of the chemical composition of the minerals on flotation was almost inextricably bound up with particle morphology and emphasizes the importance of considering both factors and investigating them individually for the flotation study.

3. MATERIALS AND METHODS

3.1. Samples and Chemicals. Lauraphos301 (28.5% [(dodecylimino)bis(methylene)]bisphosphonic acid, Zschimmer & Schwarz GmbH & Co. KG) was used as received. Hydrochloric acid (~37%) and sodium hydroxide (≥99%) were used to adjust the pH, and potassium chloride was used to prepare the background solutions.

3.2. Chemical Properties of Diphosphonic Acid Lauraphos301. Based on the titration measurement, the dissociation constants of Lauraphos301 are pK_{a1} = 6.8 and pK_{a2} = 8.8 (Figure 11). The chemical structure of Lauraphos301 is shown in Figure 12.

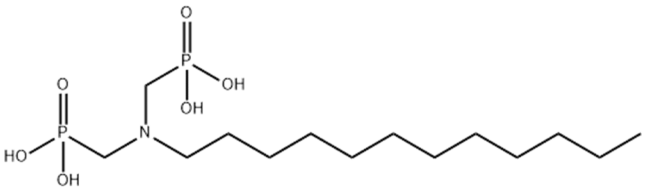

Figure 12. Chemical structure of [(dodecylimino)bis(methylene)]-bisphosphonic acid.

3.3. Cassiterite Synthesis by Sintering. Very pure SnO_2 powder (>99.99%, particle size <10 μm) was used for sintering larger pure cassiterite crystals. For the sample doped with Fe_2O_3, 2−3 wt % Fe_2O_3 powder with purity ≥99.9% was mixed with the pure SnO_2 powder. To mix the two powders homogeneously, the samples doped with Fe_2O_3 were put in the laboratory mixer mill (MM 400, Retsch) to shake for 5 min before pressing into pellets. During the pressing procedure, the samples underwent a pressure of 35 kN for 2 min. The pressed samples were placed into corundum crucibles and heated up to 1700 °C for 10 h under a normal atmosphere. After cooling down to 20 °C for 2 h, the samples were crushed, ground, milled, and classified via wet sieving to collect the −40 μm + 32 μm fraction. Wet sieving was repeated several times until the sieved water was transparent with the last wet sieving using distilled water so that the possibility of the existence of any form of leftover ions was largely minimized (Figure 13).

3.4. Sample Characterization Methods. Pure cassiterite was analyzed using several analytical methods, including optical microscopy, scanning electron microscopy (SEM) combined with energy-dispersive X-ray (EDX) analysis, and X-ray powder diffraction (XRD).

For the XRD measurement, only pure cassiterite and cassiterite doped with a low Fe content were measured, as the measurement aims at investigating Fe substitution in the cassiterite lattice.

The X-ray diffractometer (PANalytical Empyrean) was run in the reflection mode with Co Kα radiation (tube potential = 35 kV and tube current = 35 mA). The diffraction patterns with a 0.0131° 2θ step size measurements were conducted from 5 to 80°. The qualitative XRD phase identification analysis was based on the PDF-4 +2020 database (ICDD) and PANalytical HighScore 3.0.4 program and (semi-) quantitative phase identification: Profex 3.10.2 software using Rietveld refinement.[50]

For scanning electron microscopy (SEM) combined with energy-dispersive X-ray (EDX) analysis, the cassiterite particles were embedded in an epoxy block of 25 mm in diameter, ground, polished, and carbon-coated. SEM−EDX analysis was carried out using an FEI Quanta 650F field emission SEM (FE-SEM) with two Bruker Quantax X-Flash 5030 energy-dispersive X-ray (EDX) detectors at 15 kV and 1 nA probe current. The measurement time for each spot was 100 s. Standard-based quantification was used. Spectra processing and quantification were performed with the software package DTSA-II, version Lorentz, developed by Nicholas W.M. Ritchie (NIST). The simplified XPP algorithm according to Pouchou and Poichoir[51]

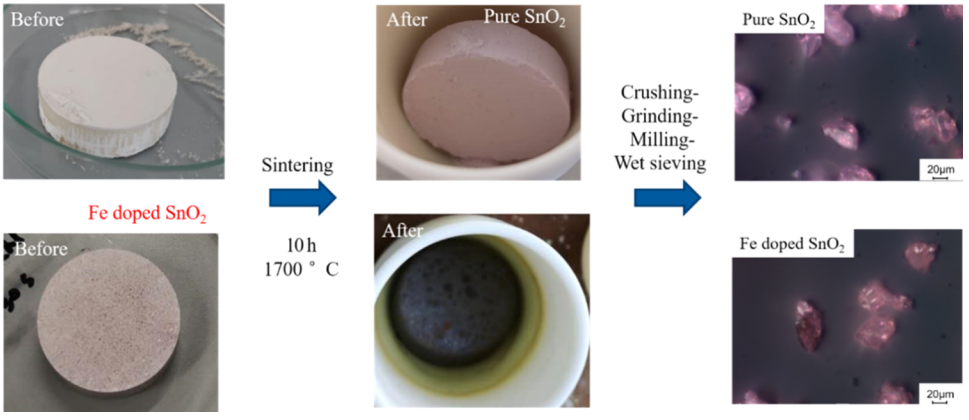

Figure 13. Sample production procedure starts with sintering followed by crushing, grinding with pestle and mortar, milling with a planetary ball mill, and wet sieving for target particle size ranges.

https://doi.org/10.1021/acsomega.2c07230
ACS Omega 2023, 8, 5702−5714

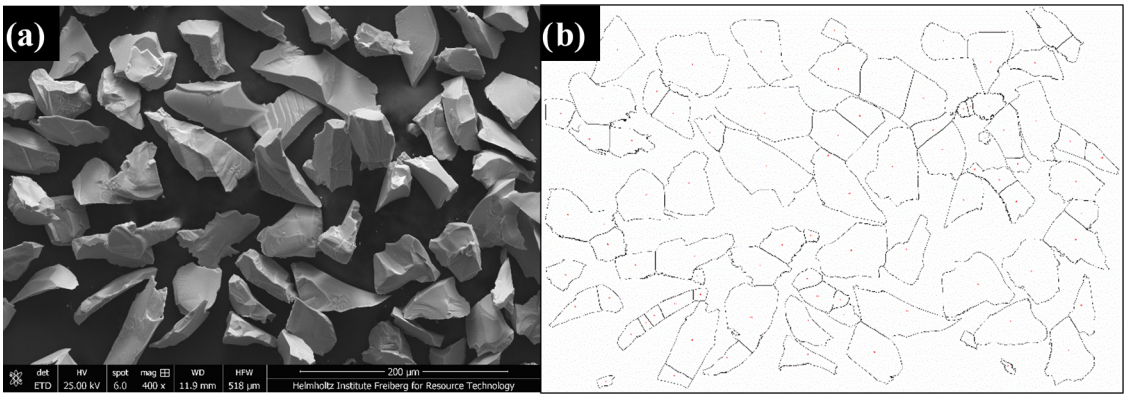

Figure 14. (a) Original secondary electron (SE) image of Fe-doped cassiterite samples. (b) The processed image after analysis in Image J software.

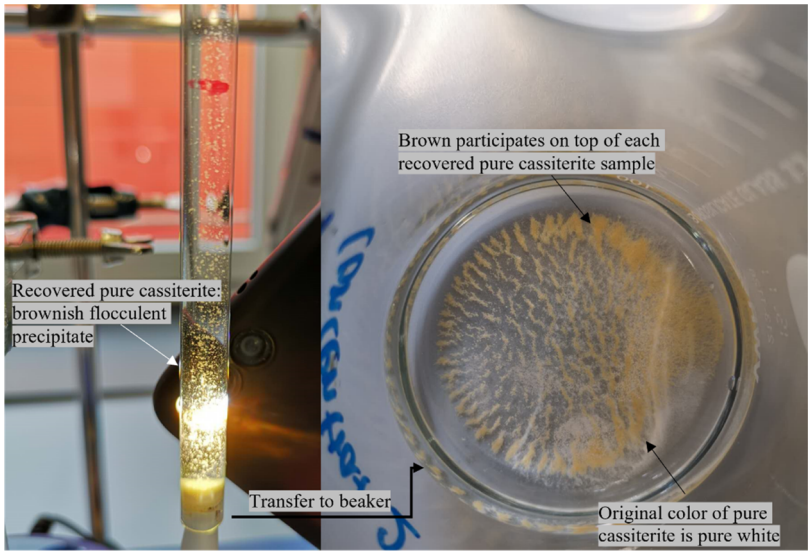

Figure 15. Pure cassiterite recovered in the Hallimond tube (left) during microflotation and transferred to the beaker (right) after the microflotation experiment. A loosely constructed brownish layer can be seen on the top of the recovered pure cassiterite, which indicates the generation of iron phosphonate complexes on the particle surfaces.

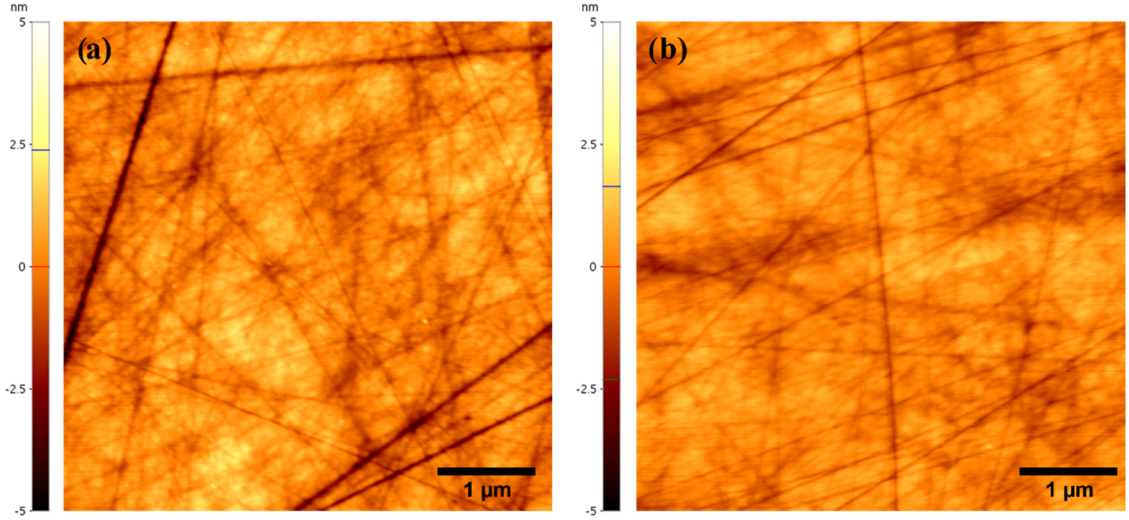

Figure 16. AFM topography of (a) pure cassiterite and (b) cassiterite with 1417 ppm Fe.

was used as the correction algorithm. The mass absorption coefficients were taken from Pouchou and Poichoir.[51] The elements O, Sn, Fe, Mn, Nb, Ta, W, and Ti were included in the quantification. The respective ASTM metal standards were used. All measurements were corrected to a carbon-coating of 15 nm

https://doi.org/10.1021/acsomega.2c07230
ACS Omega 2023, 8, 5702−5714

Table 2. Compilation of All SEM−EDX Measurement Data[a]

	Sn		O		Fe		mea. con.	
sample	nor. wt %	unc.	nor. wt %	unc.	nor. wt %	unc.	LT (S)	ac. vol. (V)
Cass-Fe-1.	0.2137	0.0023	0.785	0.0034	0.0013	0.0005	97.2	15.051
Cass-Fe-2.	0.2172	0.0023	0.7821	0.0034	0.0007	0.0005	97.1	15.046
Cass-Fe-3.	0.2135	0.0023	0.7853	0.0033	0.0012	0.0004	97.3	15.068
Cass-Fe-4.	0.2173	0.0023	0.7809	0.0034	0.0017	0.0005	97.2	15.002
Cass-Fe-5.	0.2163	0.0016	0.7822	0.0034	0.0014	0.0005	97.2	15.030
Cass-Fe-6.	0.2158	0.0023	0.7831	0.0034	0.001	0.0004	97.2	15.035
Cass-Fe-7.	0.2106	0.0023	0.7881	0.0033	0.0013	0.0005	97.1	14.986
Cass-Fe-8.	0.2186	0.0023	0.7793	0.0034	0.0021	0.0005	97.2	15.037
Cass-Fe-9.	0.2146	0.0023	0.7836	0.0034	0.0018	0.0005	97.3	15.000
Cass-Fe-10.	0.2178	0.0023	0.7806	0.0034	0.0015	0.0004	97.2	15.086
Cass-Fe-11.	0.2180	0.0023	0.7802	0.0034	0.0018	0.0005	97.1	15.064
Cass-Fe-12.	0.2138	0.0023	0.7844	0.0034	0.0018	0.0005	97.2	15.014
Cass-Fe-13.	0.2137	0.0023	0.7853	0.0034	0.0010	0.0005	97.1	14.970
Cass-Fe-14.	0.2123	0.0023	0.7868	0.0033	0.0009	0.0005	97.2	15.102
Cass-Fe-15.	0.2160	0.0023	0.7828	0.0034	0.0012	0.0004	97.1	15.014
Fe average 0.001417								
Cass-Fe-low_1.	0.2108	0.0023	0.7879	0.0033	0.0013	0.0005	97.1	15.021
Cass-Fe-low_2.	0.2138	0.0023	0.7855	0.0034	0.0006	0.0005	97.3	15.039
Cass-Fe-low_3.	0.2128	0.0023	0.7862	0.0033	0.0009	0.0005	97.2	15.055
Cass-Fe-low_4.	0.2157	0.0023	0.7827	0.0034	0.0017	0.0005	97.2	15.049
Cass-Fe-low_5.	0.2148	0.0023	0.7842	0.0034	0.0012	0.0005	97.3	15.031
Cass-Fe-low_6.	0.2125	0.0023	0.7868	0.0034	0.0007	0.0005	97.2	14.997
Cass-Fe-low_7.	0.207	0.0022	0.7921	0.0033	0.001	0.0005	97.1	14.985
Cass-Fe-low_8.	0.2068	0.0022	0.7921	0.0033	0.0012	0.0005	97.1	14.972
Cass-Fe-low_9.	0.2073	0.0022	0.7913	0.0033	0.0015	0.0005	97.2	15.012
Cass-Fe-low_10.	0.208	0.0023	0.7906	0.0033	0.0014	0.0005	97.2	14.986
Cass-Fe-low_11.	0.2107	0.0023	0.7882	0.0034	0.0013	0.0005	97.2	14.991
Cass-Fe-low_12.	0.2125	0.0023	0.7869	0.0034	0.0005	0.0005	97.2	14.991
Cass-Fe-low_13.	0.2111	0.0023	0.7882	0.0033	0.0008	0.0005	97.2	15.028
Cass-Fe-low_14.	0.2133	0.0023	0.7854	0.0034	0.0013	0.0005	97.2	14.963
Cass-Fe-low_15.	0.2179	0.0023	0.78	0.0034	0.0021	0.0005	97.2	15.043
Fe average 0.001165								

[a]Nor., wt %, Unc., LT, and Ac. Vol. stand for normalized, mass fraction, uncertainty, live time, and acceleration voltage, respectively.

thickness. All elements except Sn, O, and Fe were below the detection limit of the method.

In addition, the particle shape acquired by secondary electron (SE) imaging was analyzed using Image J software. During the image processing, the threshold of each picture was selected based on the color difference of the particle contours. The particles at the edge of the SE images were eliminated to avoid false particle shape identification. Settings like the range of selected area and perimeter were adjusted. Figure 14a,b illustrates one example of the SE image before and the processed image afterward.

In this study, only the roundness values were used to evaluate the particle shape due to its significant influence on the bubble−particle and particle−particle interactions.[43] With the help of the measured perimeter P and area A, the roundness R of each particle can be calculated as follows

$$R = \frac{4 \cdot \pi \cdot A}{P^2} \quad (1)$$

3.5. Microflotation. Single mineral microflotation was carried out using the 32−40 μm fraction. The cassiterite sample (1 g) was first submerged in the 190 mL 1×10^{-2} mol/L KCl solution. For the measurement without ferric ions in the solution, the system was adjusted to the target pH with either HCl or NaOH. After the pH adjustment, the collector was added. The condition time remained 5 min. For the measurement with ferric ions, $FeCl_3 \cdot 6H_2O$ (purity ≥ 97%) was chosen as the Fe^{3+} source. Then, 2×10^{-4} mol/L Fe^{3+} was added to the solution, followed by the addition of the collector. The solution was further adjusted to the target pH, and the condition time remained 5 min.

Afterward, the samples were transferred to the Hallimond tube,[52] which was designed by TU Bergakademie Freiberg. The transfer of the sample took 2 min. An additional 3 min of conditioning in the tube resulted in a total conditioning time of 10 min before the flotation began. For the flotation, the airflow was set to 40 cm^3 min^{-1} for 2 min. The Hallimond tube was equipped with a magnetic stirrer rotating at 800 rpm during the 10 min conditioning time and at 600 rpm during the 2 min flotation time.

The concentrate and tailings were collected separately on a filter, extensively rinsed with deionized (DI) water, and dried at 50−60 °C until mass constancy was reached. The resulting mass balance was checked for losses, and results with losses above 10% were excluded from the data evaluation.

3.6. Electrophoretic Mobility Measurements. Electrokinetic behaviors of synthetic cassiterite were characterized by electrophoretic mobility measurements, which were carried out with a Zetasizer Nano (Malvern Panalytical). For sample preparation, 0.1 g/L particles were diluted in the background

https://doi.org/10.1021/acsomega.2c07230
ACS Omega 2023, 8, 5702−5714

KCl solution. To verify the correction of the data points, each sample was tested in a 10 mM KCl solution. After the dispersion step, the mixture was stirred and tempered to 25 °C for 15 min, and the pH value was set utilizing HCl or KOH.

To define the suitable kinetic model, the particle size distribution of each measured sample was additionally determined using a laser diffraction particle size analyzer (HELOS, Sympatec GmbH). The mean value of the measured particle size was defined as the curvature radius a. Based on Smoluchowski's theory, which is valid for $\kappa a \gg 1$, the calculated values of κa were all larger than 100, which is in the large κa regime.[53] The simple analytical model O'Brien-White equation was applied for the determination of the ζ-potential

$$\frac{3}{2}\frac{\eta e}{\varepsilon_{rs}\varepsilon_0 kT}u_e = \frac{3}{2}y^{ek} - \frac{6\left[\frac{y^{ek}}{2} - \frac{\ln 2}{z}\left(1 - e^{-zy^{ek}}\right)\right]}{2 + \frac{\kappa a}{1 + 3mz^{-2}}e^{-zy^{ek}/2}} \quad (2)$$

where $y^{ek} = \frac{e\zeta}{kT}$, u_e is the electrophoretic mobility, and η is the dynamic viscosity.

3.7. Topographic Imaging and Roughness Quantification Using Atomic Force Microscopy (AFM). To achieve similar roughness after polishing, the cassiterite samples used for the AFM measurement were all embedded in the same epoxy resin block. The AFM measurements were carried out with an XE-100 (Park Systems), including topographic imaging and roughness quantification. The topography of the untreated cassiterite samples as well as cassiterite samples treated with 1×10^{-4} mol/L Lauraphos301 at pH 6 was investigated by AFM. For the adsorption analysis, the epoxy resin block containing both pure cassiterite and cassiterite with 1417 ppm Fe was immersed into the 10 mmol/L KCl solution with 1×10^{-4} mol/L Lauraphos301 at pH 6 for 5 min. Before the topography analysis, the sample was removed from the solution and blown dry with air.

APPENDIX

(Lorentz) (Figures 15 and 16A, Table 2).

All SEM−EDX measurements were performed standard-based at a 15 keV accelerating voltage and 1 nA beam current. The correction calculations were performed according to the simplified XPP method of Pouchou & Pichoir using DTSA-II. The quantified data are calculated as "normalized mass fraction" for better comparability. The sums of the "mass fraction" of all measurements are between 100 and 103 weight %.

The measurement uncertainties were determined from the "mass fractions" as combined uncertainties at the 1 s level and converted to the "normalized mass fraction". These combined uncertainties are composed of intensity ratios (standard | unknown); count statistics of (standard| unknown); absorption correction; and Backscatter correction.

The SEM measurement parameters live time (LT), accelerating voltage, and beam current were determined for each measurement and are listed individually.

AUTHOR INFORMATION

Corresponding Author

Haosheng Wu − *Helmholtz-Zentrum Dresden-Rossendorf (HZDR), Helmholtz Institute Freiberg for Resource Technology (HIF), 09599 Freiberg, Germany*; orcid.org/0000-0001-6979-2243; Email: haosheng.wu@hzdr.de

Authors

Doreen Ebert − *Helmholtz-Zentrum Dresden-Rossendorf (HZDR), Helmholtz Institute Freiberg for Resource Technology (HIF), 09599 Freiberg, Germany*

Robert Möckel − *Helmholtz-Zentrum Dresden-Rossendorf (HZDR), Helmholtz Institute Freiberg for Resource Technology (HIF), 09599 Freiberg, Germany*

Kai Bachmann − *Helmholtz-Zentrum Dresden-Rossendorf (HZDR), Helmholtz Institute Freiberg for Resource Technology (HIF), 09599 Freiberg, Germany*

Axel D. Renno − *Helmholtz-Zentrum Dresden-Rossendorf (HZDR), Helmholtz Institute Freiberg for Resource Technology (HIF), 09599 Freiberg, Germany*; orcid.org/0000-0002-8289-1059

Martin Rudolph − *Helmholtz-Zentrum Dresden-Rossendorf (HZDR), Helmholtz Institute Freiberg for Resource Technology (HIF), 09599 Freiberg, Germany*

Complete contact information is available at: https://pubs.acs.org/10.1021/acsomega.2c07230

Notes

The authors declare no competing financial interest.

ACKNOWLEDGMENTS

The authors would like to thank the Program-oriented Funding (POF) of the Helmholtz Association for supporting the project. The authors would like to thank Sabine Gilbricht and Kristine Trinks for operating the SEM−EDX measurements; the authors would also like to thank Klaus Graebe for the measurement of particle size distribution, Anja Östereich for titration measurement, Arsenii Rybalchenko, Sebastian Barajas, Volker Rechksiek, Yi Zou, and Mohammed Omar Sahed Chowdhury for sample preparation.

REFERENCES

(1) Drzymala, J.*Mineral Processing: Foundations of Theory and Practice of Minerallurgy*; University of Technology, 2007.

(2) Sutherland, K. L.; Wark, I. W.*Principles of Flotation*; Australasian Institute of Mining and Metallurgy, 1955.

(3) Schubert, H.*Aufbereitung Fester Mineralischer Rohstoffe Band III*, VEB Deutscher Verlag für Grundstoffindustrie: 1984; Vol. *53*.

(4) Rao, R.; Leja, J.*Surface Chemistry of Froth Flotation. Volume 1, Fundamentals*; Springer Science & Business Media, 2004; Vol. *1*.

(5) Bulatovic, S. M.Flotation of Tin Minerals. In *Handbook of Flotation Reagents: Chemistry, Theory and Practice*, Bulatovic, S. M., Ed.; Elsevier: Amsterdam, 2010; pp 87−109.

(6) Fuerstenau, D. W.; Modi, H. J. Streaming Potentials of Corundum in Aqueous Organic Electrolyte Solutions. *J. Electrochem. Soc.* **1959**, *106*, 336−341.

(7) Rai, B.; Sathish, P.; Tanwar, J.; Pradip; Moon, K. S.; Fuerstenau, D. W. A Molecular Dynamics Study of the Interaction of Oleate and Dodecylammonium Chloride Surfactants with Complex Aluminosilicate Minerals. *J. Colloid Interface Sci.* **2011**, *362*, 510−516.

(8) Choi, W. Z.; Jeon, H. S.; Zeng, Q.; Jiang, E.; Wang, D. Influence of Metal Cations on Cassiterite Flotation. *Geosystem Eng.* **1998**, *1*, 53−57.

(9) Feng, Q.; Zhao, W.; Wen, S.; Cao, Q. Activation Mechanism of Lead Ions in Cassiterite Flotation with Salicylhydroxamic Acid as Collector. *Sep. Purif. Technol.* **2017**, *178*, 193−199.

(10) Feng, Q.; Wen, S.; Zhao, W.; Chen, H. Interaction Mechanism of Magnesium Ions with Cassiterite and Quartz Surfaces and Its Response to Flotation Separation. *Sep. Purif. Technol.* **2018**, *206*, 239.

(11) Fuerstenau, M. C.; Lopez-Valdivieso, A.; Fuerstenau, D. W. Role of Hydrolyzed Cations in the Natural Hydrophobicity of Talc. *Int. J. Miner. Process.* **1988**, *23*, 161−170.

https://doi.org/10.1021/acsomega.2c07230
ACS Omega 2023, 8, 5702−5714

(12) Schröcke, H.Sächsische Zinnlagerstätten, Ihre Paragenesen Und Altersstellung. *Vor. des berg- und hüttenmännischen Tages1951***1952**.
(13) Fischer, J.*Untersuchungen über die Beziehungen zwischen Physikalischen und Chemischen Eigenschaften von Zinnstein Verschiedener Lagerstätten Und Seiner Flotierbarkeit*; Technische Universität Dresden, 1967.
(14) Schneider, H. J.; Dulski, P.; Luck, J.; Möller, P.; Villalpando, A. Correlation of Trace Element Distribution in Cassiterites and Geotectonic Position of Their Deposits in Bolivia. *Miner. Depos.* **1978**, *13*, 119−122.
(15) Cheng, Y.; Spandler, C.; Kemp, A.; Mao, J.; Rusk, B.; Hu, Y.; Blake, K. Controls on Cassiterite (SnO2) Crystallization: Evidence from Cathodoluminescence, Trace-Element Chemistry, and Geochronology at the Gejiu Tin District. *Am. Mineral.* **2019**, *104*, 118−129.
(16) Gruner, H.; Bilsing, U. Cassiterite Flotation Using Styrene Phosphonic Acid to Produce High-Grade Concentrates at High Recoveries from Finely Disseminated Ores- Comparison with Other Collectors and Discussion of Effective Circuit Configurations. *Miner. Eng.* **1992**, *5*, 429−434.
(17) Noll, W.Zur Kristallchemie Des Zinnsteins (Kassiterit). *Mineral. Inst. der Tech. Hochschule Darmstadt***1944**.
(18) Jańczuk, B.; González-Martín, M. L.; Bruque, J. M. Wettability of Cassiterite in Presence of Sodium Dodecyl Sulphate. *Mater. Chem. Phys.* **1994**, *38*, 225−233.
(19) Senior, G. D.; Poling, G. W.; Frost, D. C. Surface Contaminants on Cassiterite Recovered from an Industrial Concentrator. *Int. J. Miner. Process.* **1989**, *27*, 221−242.
(20) Wottgen, V. E.; Luft, D.; Neuber, C.; Rosenbaum, C.Der Einsatz Regelnder Reagenzien in Der Kassiteritflotation. *Freib. Forschungshefte***1975**, *A551*.
(21) Senior, G. D.The Role of Dissolved Metal Ionic Species in the Phosphonic Acid Flotation of Cassiterite, Dissertation. University of British Columbia, 1987.
(22) Schumann, R.; Prakash, B.*Minerals Engineering*, 1950.
(23) Sutherland, K. L.; Wark, I. W.*Principles of Flotation*; Melbourne: Australasian Institute of Mining and Metallurgy, 1950.
(24) Gruner, H.*Untersuchung des Einflusses von Fremdelementbeimengungen in Synthetischen Zinnstein auf die Flotationseigenschaften von Zinnstein*; TU Bergakademie Freiberg, 1969.
(25) Balachandran, S. B.; Simkovich, G.; Aplan, F. F. The Influence of Point Defects on the Floatability of Cassiterite, I. Properties of Synthetic and Natural Cassiterites. *Int. J. Miner. Process.* **1987**, *21*, 157−171.
(26) Vaziri Hassas, B.; Caliskan, H.; Guven, O.; Karakas, F.; Cinar, M.; Celik, M. S. Effect of Roughness and Shape Factor on Flotation Characteristics of Glass Beads. *Colloids Surf., A* **2016**, *492*, 88−99.
(27) Chau, T. T.; Bruckard, W. J.; Koh, P. T. L.; Nguyen, A. V. A Review of Factors That Affect Contact Angle and Implications for Flotation Practice. *Adv. Colloid Interface Sci.* **2009**, *150*, 106−115.
(28) Shannon, R. D. Revised Effective Ionic Radii and Systematic Studies of Interatomic Distances in Halides and Chalcogenide. *Acta Crystallogr. Sect. A Cryst. physics, diffraction, Theor. Gen. Crystallogr.* **1976**, *32*, 751−767.
(29) Dietze, U. Infrarotspektroskopische Untersuchungen zum Anlagerungsmechanismus von Phosphon- und Arsonsäuren an Kassiterit bei dessen Flotation. *Freib. Forschungshefte* **1975**, *446*, 1−38.
(30) Collins, D. N.; Kirkup, J. L.; Davey, M. N.; Arthur, C.Flotation of Cassiterite. Development of a Flotation Process. *Trans. Inst. Miner. Metall.***1968**.
(31) E Töpfer, H.; Gruner, U. B. Untersuchung ueber das Flotationsverhalten von Kassiterit. *Freib. Forschungshefte* **1975**, 39−52.
(32) Houot, R.; Desbrosses, Y. Is the Cassiterite Contained in Complex Sulphide Polymetallic Ore Recoverable? *Int. J. Miner. Process.* **1991**, *32*, 45−57.
(33) Wu, H.; Renno, A. D.; Martin Rudolph In The Influence of Fe as Trace Element on the Floatability of Cassiterite. Stage One: Sample Property of the Synthetic and Natural Cassiterite and First Test of Their Flotation Behavior, *IMPC 2020:XXX International Mineral Processing Congress*, 2020.
(34) Houchin, M. R.; Warren, L. J. Surface Titrations and Electrokinetic Measurements on Stannic Oxide Suspensions. *J. Colloid Interface Sci.* **1984**, *100*, 278−286.
(35) Fuerstenau, D. W.; Pradip. Zeta Potentials in the Flotation of Oxide and Silicate Minerals. *Adv. Colloid Interface Sci.* **2005**, *114−115*, 9−26.
(36) Somasundaran, P.; Healy, T. W.; Fuerstenau, D. W. Surfactant Adsorption at the Solid-Liquid Interface - Dependence of Mechanism on Chain Length. *J. Phys. Chem. A* **1964**, *68*, 3562−3566.
(37) Fuerstenau, D. W.; Colic, M. Self-Association and Reverse Hemimicelle Formation at Solid-Water Interfaces in Dilute Surfactant Solutions. *Colloids Surf., A* **1999**, *146*, 33−47.
(38) Farrow, J. B.; Warren, L. J. Adsorption of Short-Chained Organic Acids on Stannic Oxide. *Colloids Surf.* **1988**, *34*, 255−269.
(39) Wottgen, E.; Dietze, U. Über Die Anlagerung von Phosphonsäuren an Kassiterit Bei Der Flotation. *Zeitschrift für Anorg. und Allg. Chemie* **1969**, 64−72.
(40) Gruner, H. Untersuchung Des Einflusses von Fremdelementbeimengungen in Synthetischen Zinnstein Auf Die Flotationseigenschaften von Zinnstein. *Freib. Forschungshefte* **1971**, *A499*, 7−23.
(41) Fuerstenau, D. W.; Healy, T. W.Principles of Mineral Flotation. In *Adsorptive Bubble Separation Techniques*, Academic Press: 1972; pp 91−131.
(42) Kuys, K. J.; Roberts, N. K. In Situ Investigation of the Adsorption of Styrene Phosphonic Acid on Cassiterite by FTIR-ATR Spectroscopy. *Colloids Surf.* **1987**, *24*, 1−17.
(43) Uysal, T.; Guven, O.; Ozdemir, O.; Karaagaclioglu, E.; Tunç, B.; Çelik, M. S. Contribution of Particle Morphology on Flotation and Aggregation of Sphalerite Particles. *Miner. Eng.* **2021**, *165*, No. 106860.
(44) Varela, J. A.; Perazolli, L. A.; Longo, E.; Leite, E. R.; Cerri, J. A. Effect of Atmosphere and Dopants on Sintering of SnO2. *Radiat. Eff. Defects Solids* **1998**, *146*, 131−143.
(45) Vaziri Hassas, B.; Caliskan, H.; Guven, O.; Karakas, F.; Cinar, M.; Celik, M. S. Effect of Roughness and Shape Factor on Flotation Characteristics of Glass Beads. *Colloids Surf., A* **2016**, *492*, 88−99.
(46) Guven, O.; Karakas, F.; Kodrazi, N.; Çelik, M. S. Dependence of Morphology on Anionic Flotation of Alumina. *Int. J. Miner. Process.* **2016**, *156*, 69−74.
(47) Ulusoy, U.; Yekeler, M.; Hiçyilmaz, C. Determination of the Shape, Morphological and Wettability Properties of Quartz and Their Correlations. *Miner. Eng.* **2003**, *16*, 951−964.
(48) Guven, O.; Serdengecti, M. T.; Tunc, B.; Ozdemir, O.; Karaagaclioglu, I. E.; Çelik, M. S. Effect of Particle Shape Properties on Selective Separation of Chromite from Serpentine by Flotation. *Physicochem. Probl. Miner. Process.* **2020**, *56*, 818−828.
(49) Han, K. N.; Healy, T. W.; Fuerstenau, D. W. The Mechanism of Adsorption of Fatty Acids and Other Surfactants at the Oxide-Water Interface. *J. Colloid Interface Sci.* **1973**, *44*, 407−414.
(50) Doebelin, N.; Kleeberg, R. Profex: A Graphical User Interface for the Rietveld Refinement Program BGMN. *J. Appl. Crystallogr.* **2015**, *48*, 1573−1580.
(51) Pouchou, J.-L.; Pichoir, F.Quantitative Analysis of Homogeneous or Stratified Microvolumes Applying the Model "PAP". In *Electron Probe Quantitation*, Heinrich, K. F. J.; Newbury, D. E., Eds.; Springer US: Boston, MA, 1991; pp 31−75.
(52) Schubert, H. 30 Years Development in Mineral Processing - Part 1. *Aufbereitungs-Technik* **1989**, *30*, 3−14.
(53) Delgado, A. V.; González-Caballero, F.; Hunter, R. J.; Koopal, L. K.; Lyklema, J. Measurement and Interpretation of Electrokinetic Phenomena. *J. Colloid Interface Sci.* **2007**, *309*, 194−224.

https://doi.org/10.1021/acsomega.2c07230
ACS Omega 2023, 8, 5702−5714